Chirality **WILEY**

Understanding laser desorption with circularly polarized light

Florian Ristow[1] | Jakob Scheffel[1] | Xuqiang Xu[2] | Natalie Fehn[2] |
Katrin E. Oberhofer[1] | Johann Riemensberger[1] | Farinaz Mortaheb[2] |
Reinhard Kienberger[1] | Ulrich Heiz[2] | Aras Kartouzian[2] (ORCID) | Hristo Iglev[1]

[1]Physik-Department E11, Technische Universität München, Garching, Germany

[2]Catalysis Research Center and Chemistry Department, Physical Chemistry, Technical University of Munich, Garching, Germany

Correspondence

Aras Kartouzian, Catalysis Research Center and Chemistry Department, Physical Chemistry, Technische Universität München, Lichtenbergstr, 4, 85748 Garching, Germany.
Email: aras.kartouzian@mytum.de

Hristo Iglev, Physik-Department E11, Technische Universität München, James-Franck-Str. 1, D-85748 Garching, Germany.
Email: hristo.iglev@ph.tum.de

Abstract

We present aspects of emerging optical activity in thin racemic 1,1′-Bi-2-naphthol films upon irradiation with circularly polarized light and subsequent resonant two-photon absorption in the sample. Thorough analysis of the sample morphology is conducted by means of (polarization-resolved) optical microscopy and scanning electron microscopy (SEM). The influence of crystallization on the nonlinear probing technique (second harmonic generation circular dichroism [SHG-CD]) is investigated. Optical activity and crystallization are brought together by a systematic investigation in different crystallization regimes. We find crystallization to be responsible for two counter-acting effects, which arise for different states of crystallization. Measuring crystallized samples offers the best signal-to-noise ratio, but it limits generation of optical activity due to self-assembly effects. For suppression of crystallization on the other hand, there is a clear indication that enantiomeric selective desorption is responsible for the generation of optical activity in the sample. We reach the current resolution limit of probing with SHG-CD, as we suppress the crystallization in the racemic sample during desorption. In addition, intensity-dependent measurements on the induced optical activity reveal an onset threshold (≈ 0.7 TW cm^{-2}), above which higher order nonlinear processes impair the generation of optical activity by desorption with CPL.

KEYWORDS

laser desorption, preparative separation, SHG-CD

[This article is part of the Special Issue: Chirality @ The Nanoscale. See the first article for this special issue previously published in Volume 32:7. More special articles will be found in this issue as well as in those to come.]

1 | INTRODUCTION

Chirality is all around and within us—it is in our DNA and shows itself in the arrangement of cosmic structures. The interest in the phenomenon has always been high for various reasons. From a fundamental scientific point of view, for example, research has been done on the origin of life with regard to the observed homochirality,[1–4] or from an industrial point of view, where concepts like chiral sensing, asymmetric synthesis, enantiomeric purification, and asymmetric catalysis are currently of interest.[5–9] However, there are still many aspects of the phenomenon that despite remarkable progress are not sufficiently understood. Subjects of on-going research include extensively investigated topics such as parity violation or more recent concepts like chirality-induced spin selection (CISS).[10–15] Recently, we reported on the observation of the emergence of optical activity in racemic films of 1,1′-bi-2-naphthol (BINOL) after laser desorption with circularly polarized light (CPL).[16] This observation can be briefly summarized as follows: When a racemic film of BINOL molecules is exposed to CPL with energies above the desorption threshold, the anisotropy factor Δg of the remaining film shows a clear correlation with the handedness of the CPL used for desorption.

Although the phenomenon itself has been experimentally observed unambiguously, the mechanism(s) by which it happens are yet to be investigated. In a first attempt to understand the processes underlying this observation, we have previously presented a phenomenological model based on two photon absorption of ultrashort laser pulses in the film and allowing the enantiomers to possess different desorption rates when desorbed by CPL. This model suggests that the origin of the observed optical activity is the enantiomeric enrichment of the remaining film as the result of the desorption process. This in turn requires that the quantum mechanical processes play a sufficiently large role in the

desorption process to allow for chiral asymmetry. One major difficulty in confidently assigning the observed optical activity to the enantiomeric excess in the remaining film is due to the possibility of racemic mixtures to form macroscopic optically active structures. Thus, the structural properties of the film also need to be considered in order to account for their contribution to the measured optical activity on the macroscopic level.

In this contribution, we address the following two issues based on additional experimental data. By investigating the crystallization state and surface roughness of the films and their impact on the nonlinear optical response, we attempt to determine the role of structural effects in the samples' observed nonlinear response and the phenomenon of asymmetric laser desorption. By systematically studying the influence of pulse intensity of the laser beam on the magnitude of the obtained optical activity that is induced by laser desorption, we attempt to better identify the optical process that leads to the emergence of optical activity in initially racemic BINOL films. Herein, we stick to the second harmonic generation (SHG) circular dichroism (SHG-CD) as our method of choice to probe the induced optical activity, as it presented itself as a sensitive and reliable method in our earlier contribution and elsewhere.[16–20]

2 | MATERIALS AND METHODS

The experimental setup is very similar to the one reported previously.[16] Herein, we present the key information for convenience of the reader and in addition, we highlight the specific steps that have been taken for the work presented in this contribution. The setup depicted in Figure 1 is based on an amplified Ti-sapphire laser system (CPA-2001, Clark-MXR Inc.), which provides 150-fs pulses with a central wavelength of 775 nm at a repetition rate of 1 kHz. Part of the output beam is used to pump a
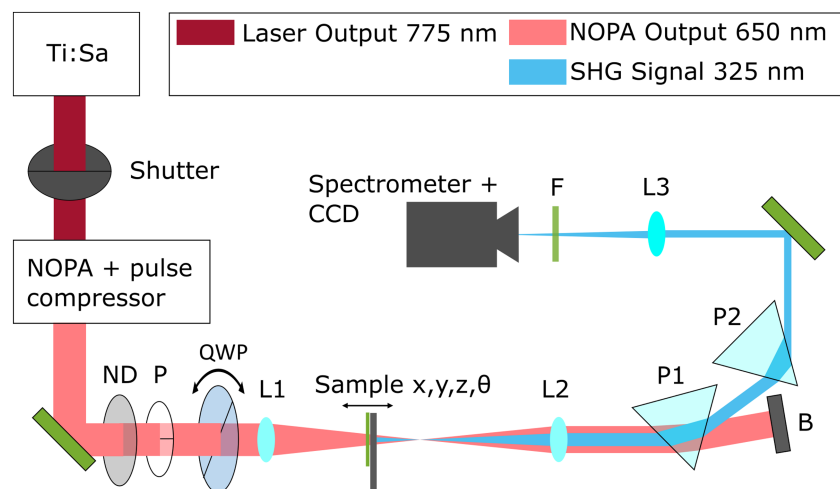

FIGURE 1 Schematic of the used experimental setup. The 775-nm laser output (red) is converted to sub 50-fs pulses at 650 nm (light red). A motorized quarter-waveplate (QWP) alters the original linear polarization of the incident laser light to circular polarized light. The second harmonic (blue) is spatially separated from the fundamental by two prisms and guided into the detector setup

noncollinear optical parametric amplifier (NOPA), which in combination with a prism compressor yields pulses centered at 650 nm with duration t_p = 50 fs and a typical spectral with of $\Delta\lambda_{Fund}$ = 77 nm (see Figure S1A). A wire-grid polarizer (P) ensures linear polarization of the NOPA output, while a subsequent continuously variable neutral density filter (ND) facilitates precise control of the pulse energy E_p. After that, a motor-driven quarter-waveplate (QWP) is used to adjust the polarization of the excitation light to right circular polarized (RCP) or left circular polarized (LCP). An external shutter blocks the laser beam during the rotation of the QWP and between the desorption steps. The excitation beam was focused on the sample via a fused silica (FS) lens. This beam serves for laser desorption of the molecular sample film and is used to monitor its optical activity via SHG-CD. Two-photon absorption (TPA) is reasonably efficient at the chosen fundamental wavelength 650 nm, and the enantiomers show different absorption strengths for the RCP fundamental, quantified by the CD (see supporting information). The studied sample was mounted on an x–y–z translation stage, whereas the incident angle on the sample is set to 90°. The size of the laser spot A and the pulse energy E_p on the sample was recalculated from a z-scan (along the beam direction). The intensity of the excitation pulse is estimated according to $I_p = E_p/(A \cdot t_p)$.

After passing the sample, the excitation beam at 650 nm and the new generated SHG signal are re-collimated by a second FS lens and spatially separated by two FS prisms. The 325 nm radiation passes two bandpass filter systems (Schott 2UG11, 1UG5) and is focused into the spectrometer (MicroHR, Horiba Scientific). The weak SHG signal is detected by a liquid nitrogen-cooled charge-coupled device (CCD) detector (LN/CCD-1340/400-EB1, Princeton Instruments Roper Scientific). The optical activity of the sample is determined from the measured (spectrally integrated) SHG intensities and expressed by the anisotropy factor:

$$g(t) = 2 \cdot \frac{I(t)^{LCP} - I(t)^{RCP}}{I(t)^{LCP} + I(t)^{RCP}}. \quad (1)$$

It should be mentioned here that the initial values of $I(t = 0)^{LCP}$ and $I(t = 0)^{RCP}$ are not necessarily identical, and thus, the initial g-value of the as-prepared samples (g_0) might deviate from zero. Accordingly, the anisotropy factor induced by the irradiation with CPL is defined as $\Delta g(t) = g(t) - g_0$. Thus, for each measured data point, Δg corrects for initial fluctuations of g_0 that may be due to the local variation of enantiomeric distribution in the sample and/or variations in the local structure of the film, that is, the arrangement of the molecules.

The investigated samples consist of thin molecular films of racemic BINOL evaporated on 0.2-mm thick FS substrates. The samples are prepared in an external vacuum chamber equipped with an organic molecular beam evaporator of in-house design. The typical film thicknesses were between 0.8 and 1.0 µm. For each measurement, a new spot was irradiated on the sample, such that an originally racemic composition of the sample can be assumed. In order to reduce the possible impact of astigmatism or local hot-spots in the spatial beam profile, the presented data are measured outside the beam focal plane.

Additional information and more methods like scanning electron microscopy (SEM), profilometry, polarization resolved microscopy, and confocal microscopy are highlighted in the supporting information.

3 | RESULTS AND DISCUSSION

3.1 | Morphology of the racemic BINOL films

It is well-known that BINOL aggregation is mainly driven by intermolecular interaction, most importantly the hydrogen bonding between hydroxyl groups.[21–23] The overall crystallization process of BINOL is rather complex and an ongoing subject of research.[24–26] Racemic BINOL crystallizes in an orthorhombic structure as opposed to enantiopure BINOL, which forms a trigonal crystal system with at least three different possible molecular conformations for each enantiomer.[27] It is expected that the morphology of the racemic BINOL film could play an important role for the SHG efficiency and in the generation of optical activity via laser desorption with CPL. To elucidate the structural changes of racemic BINOL during the crystallization process, we studied 0.85 ± 0.15-µm thin racemic BINOL films in different crystallization states and correlated these measurements with data on the surface roughness. The thickness and corresponding surface roughness R_S, defined as the RMS of the surface profile, were measured with a profilometer. Additional information on the surface profiles for different crystallization states and the retrieval of R_S is provided in the Figure S3.

After preparation, the samples were stored ex-vacuo at room temperature for different periods of time in order to allow for crystallization. The optical microscopy images presented in Figure 2A–C display the structural properties of the films with regard to the age of the sample. Figure 2A shows an image of a highly transparent fresh BINOL sample. It becomes apparent that over time, the racemic BINOL sample's opacity increases. Figure 2B was taken 2 days after evaporation. Primary crystal nucleation
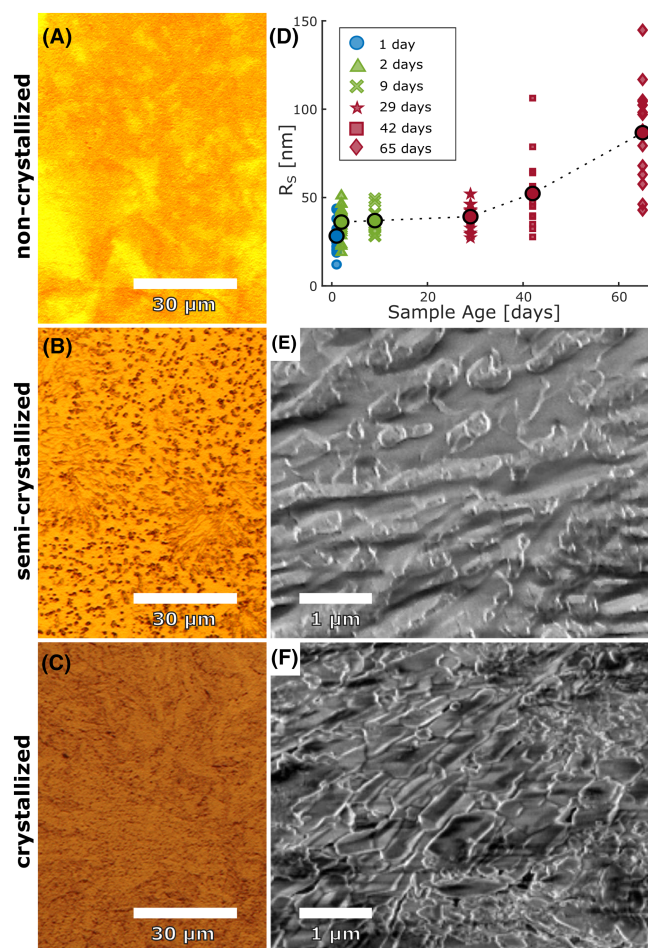
FIGURE 2 Optical reflection microscopy images to illustrate the crystallization behavior of racemic 1,1'-bi-2-naphthol (BINOL) (A) 30 min after sample preparation. The dark and blurry contours stem from the microscope work surface. (B) Two days after sample preparation. (C) Several weeks after sample preparation. (D) Surface roughness R_S versus sample age. Different colors represent the different crystallization regimes. In accordance with images B and C, scanning electron microscopy (SEM) images of (E) a semicrystallized sample, (F) a crystallized sample. Due to insufficient film conductivity, noncrystallized samples cannot be retrieved via SEM (see supporting information)

has been initiated in racemic BINOL and the racemic mixed crystal phase is evolving. Some regions appear to have crystallized more than others, but the nucleation regime predominates. Figure 2C depicts the crystallized sample, after storage at room temperature for several weeks. Our observation of increasing opacity is corroborated by an earlier study by us, where we found that, within the first 2 months, there is no measurable absorption change in the visible range upon crystallization of BINOL-film.[15] Shortly after evaporation, the sample is highly transmissive. As the sample undergoes crystallization, we observed increased opacity, which is attributed to increased scattering throughout the visible spectral range.

Our data reveal that primary nucleation of the film initiates after 2 days. The observation agrees with an earlier report by Kuroda et al.[24] on a similar system, which showed nucleation in the film after 2 days, leading to formation of a polycrystalline phase in the sample. Systematic analysis of the surface roughness R_S (Figure 2D) gives evidence that it correlates with the degree of crystallization of the BINOL film. Within the scope of this work, R_S is introduced as an easy-to-measure, accessible quantity, which allows us to track the progress of crystallization. We defined three states of crystallization based on the increase of R_S over time, namely, "noncrystallized" when $R_S < 30$ nm, "semicrystallized" when 30 nm $\leq R_S < 40$ nm and "crystallized" for $R_S \geq 40$ nm. We note that this classification is somewhat arbitrary at this point, but will be further motivated in the following section.

We also made an effort to take a closer look at the racemic samples' crystals via SEM. Figure 2E shows an SEM image of a racemic BINOL film in semicrystallized state, while Figure 2F shows an image of a crystallized film. It is well known that for organic substances such as conductive polymers, crystallization can increase the electrical conductivity by orders of magnitude due to increased order in the sample.[28,29] As SEM imaging is limited by surface charge effects due to non-sufficient electrical conductivity, non-crystallized samples could not be measured with this technique. The SEM's electron beam leads to significant charge accumulation on poorly conductive surfaces, hence inducing drastic imaging aberrations or destroying the thin film in the investigated region (see Figure S4).

However, it can be seen from the images that in semicrystallized samples (Figure 2E), crystals in the order of 0.2 μm in length, covering roughly 20% of the surface have already formed, but there are still areas where the noncrystallized BINOL dominates. Size analysis was carried out by averaging the length of more than 30 crystals. Upon crystallization, the average crystal length increases to 0.8 μm (Figure 2F). In addition, the crystallite density compared with the semicrystallized sample is increased to at least 80% of the surface area. Crystals partly overlap and homogeneously cover the surface. For crystallized samples, it is therefore highly indicative that the vast majority of molecules are bound in these crystals covering the surface. In this regard, the SEM images go along very well with the light microscopy images and reveal the underlying sample structure on the scale of the crystallite size. Note that the classification criteria depend on the physical property of interest; thus, there is not a strict separation between noncrystallized, semicrystalized, and

crystalized phase.[15] In fact, properties like the surface roughness and, as will be discussed later, the SHG efficiency still change even when the crystallite coverage is full.

It is of great interest for our work to contemplate whether the crystallites in a racemic BINOL sample consist of only one type of enantiomers (homochiral) or both (heterochiral). An et al. suggest that racemic mixtures condense on the substrate in three different ways: (a) a racemic compound in which both enantiomers are present in the same single crystal, (b) a conglomerate in which a single crystal contains only one enantiomer, but the sample as a whole is racemic, and (c) a solid solution, in which the film contains both enantiomers, but there is no orderly structure.[30] Because no orderly structure can be seen in Figure 2A, we suggest that noncrystallized racemic BINOL condenses in a solid solution shortly after evaporation. During the crystallization process, the regular structure in the sample greatly increases. At room temperature, BINOL crystallizes in its thermodynamically most stable form, a racemic compound.[23,25]

We performed polarization resolved microscopy that allows us to display the local optical activity in the sample. This linear method has lower sensitivity towards the chiroptical response of a specimen when compared with nonlinear techniques such as SHG-CD, yet it allows for qualitative investigation of optical activity in BINOL.[31,32] The procedure is illustrated in Figure S5, using the example of an enantiopure BINOL sample. Here, we compare sample images with different polarizer–analyzer configurations allowing us to display the optical activity of the investigated region in a single image. For R-BINOL (a), S-BINOL (b), and racemic BINOL (c), Figure 3 shows the raw polarization-resolved microscopy images in three different polarizer–analyzer configurations and the retrieved images for the local optical activity.

The dark lines in Figure 3A,B suggest the outlines of the enantiopure BINOL domains that have a 2D hexagonal shape, indicating the trigonal lattice system.[27] Averaged over 20 crystals, the crystal length was determined to be 282 µm for R-BINOL and 228 µm for S-BINOL. Note that for the sake of comparability of the local optical activity in Figure 3A,B, we chose to display relatively small R-BINOL crystals. However, it is known that R- and S-BINOL crystals are of different sizes, due to different impurity concentrations.[15] For more details, see Figure S6. Size analysis of >15 optically active crystalline subdomains reveal an average size of 108 µm for R-BINOL and 55 µm for S-BINOL. One key observation here is that R- and S-BINOL crystals, although enantiomerically pure, exhibit eight crystal subdomains with opposing macroscopic optical activity. This polarity reversal in crystallized enantiopure BINOL was just
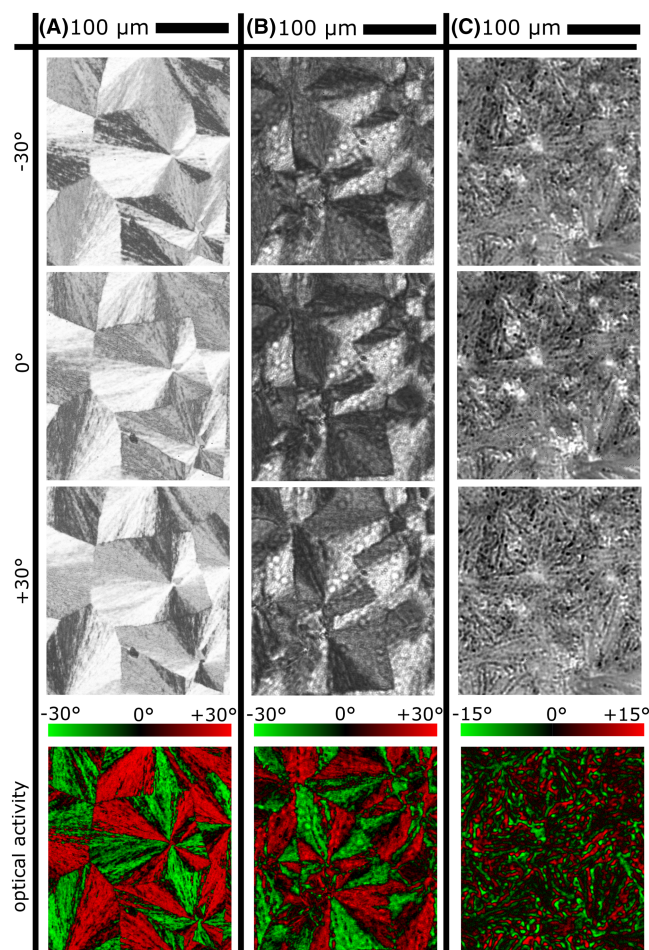

FIGURE 3 Polarization-resolved microscopy images on (A) R-, (B) S- and (C) racemic 1,1′-bi-2-naphthol (BINOL) on fused silica (FS) substrates. The analyzer is rotated by −30° (Row 1) and +30° (Row 3) from the crossed polarizer configuration 0° (Row 2). Row 4 displays the local optical activity of the sample, retrieved by the algorithm explained in the supporting information. Here, dextrorotatory (+) regions are colored red, and levorotatory (−) regions are colored green

recently confirmed by von Weber et al. and is attributed to macroscopic ordering of the molecules.[15]

For racemic BINOL (Figure 3C), the crystals are difficult to resolve, but well-pronounced elongated shapes become apparent. This observation indicates an orthorhombic crystal structure already suggested by the SEM images. Moreover, these domains mainly consist of crystals exhibiting the same sign of optical rotation. As shown in Figure 2F, racemic BINOL crystallizes in sub 1-µm crystals, whereas the length of the optically active domains in the racemic film can be estimated to be 18 µm. This strongly indicates that racemic BINOL, similarly to enantiopure BINOL, tends to form optically active super-domains. On the expense of the rotatory properties of the single enantiomers, crystal assembly appears to have a dominant effect on the chiroptical

properties of a crystallized sample as a whole. Although the literature suggests preferential crystallization in a racemic compound, analysis of the polarization resolved measurements does not allow us to unambiguously confirm this.[33] Nevertheless, this notion has great impact on our understanding of the SHG-CD measurements. Regardless of the probing technique, an enantiomerically enriched crystallized BINOL sample does not necessarily exhibit optical activity according to the predominantly represented enantiomer in the sample. Full suppression of the crystallinity in the sample is preferred, because the presence of crystal nuclei tampers the measurement of the induced anisotropy via SHG-CD.

3.2 | SHG efficiency in racemic BINOL films

To investigate the influence of the crystallization on the magnitude of the nonlinear response, the racemic BINOL samples previously prepared for the purpose of surface

roughness investigations were tested for their nonlinear response. After inserting the sample into the setup, the pulse intensity I_P was adjusted. The second harmonic intensities I_{SHG} displayed in Figure 4A,B were measured by recording 10 SHG-spectra for RCP and LCP fundamental beam in alternating order and subsequent averaging over the integrated intensities retrieved from these spectra.

In Figure 4A, the measured SHG intensities I_{SHG} have been plotted against the fundamental pulse intensities I_P, exemplary for a noncrystallized sample. As it can be expected from a nonlinear process of second order, the SHG intensity shows a quadratic dependency $I_{SHG} = C \cdot I_P^2$. The fitting constants C are shown in the inset of Figure 4B versus the surface roughness of the different samples. Figure 4b reveals that for samples with very smooth surfaces, the nonlinear response is considerably lower than for samples of which the crystallization has progressed further. As discussed later in this work, the nonlinear response from the sample limits the measurement of Δg due to the reduced experimental signal-
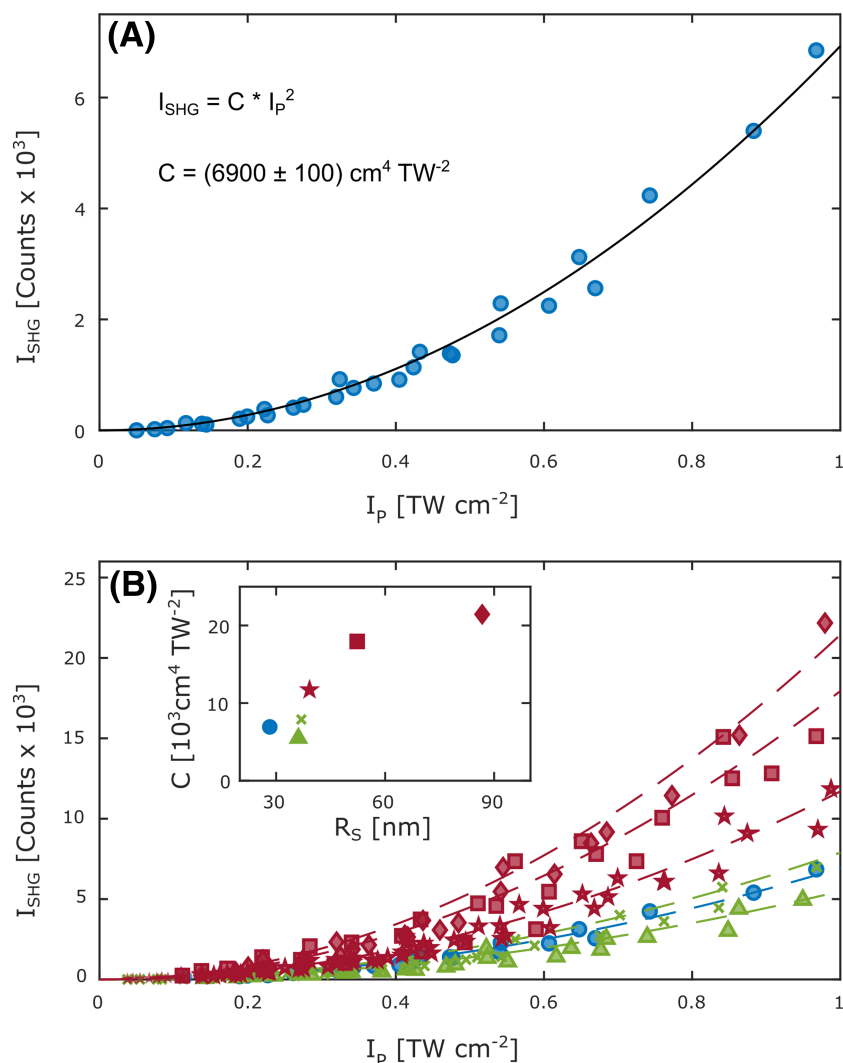

FIGURE 4 Intensity of the second harmonic generation (SHG) signal (I_{SHG}) generated in 1,1′-bi-2-naphthol (BINOL) films for different intensities of the fundamental laser pulse I_P. (A) Exemplary for the smoothest sample (blue point in the inset of Figure 4B), the measured values of I_P and the quadratic fit functions are displayed. (B) SHG intensities measured for various I_P and for a set of BINOL samples having different ages and therefore different surface roughness. The inset shows the fitting constants C for the respective surface roughness R_S. We chose the same color coding as in Figure 2D

to-noise ratios (SNRs). The increase of SHG signal as the sample undergoes crystallization is expected and commonly utilized, for example, in second-order nonlinear optical imaging of chiral crystals (SONICCs) as a measure for the crystal growth in thin films over time.[34–36] We note however that the values for $\mathbf{I_{SHG}}$ and the fitting constant $\mathbf{C}$ must be taken with extra care. Although the second harmonic is by nature eligible to probe-adsorbed chiral molecules on thin-film surfaces, in which inversion symmetry is inherently broken, we expect additional contributions to the SHG signal from spontaneously generated crystallite interfaces within the bulk of the film.[37] This process is further complicated by the shift between the surface and bulk contribution as the crystallization in the film progresses.

3.3 | Influence of the sample morphology on the generated optical activity via desorption with CPL

Given the small chiroptical response that is expected from a micron-scale molecular film, we used SHG-CD with a chiroptical sensitivity of at least three orders of magnitude higher than its linear counterpart.[31,38–40] By controlling the progress of the crystallization in the sample, it is possible to study the influence of the sample structure on the detected optical activity. As described above, the parameter of control is the time passed between the preparation of the sample and the measurement.

In this context, the initial anisotropy factor $\mathbf{g_0}$ was statistically investigated on racemic BINOL samples with respect to the influence of the crystallization state of the sample during the measurement. The data were collected from a total of more than 250 different local spots at 13 BINOL samples with various states of crystallization (defined in accordance with Figure 2B). Figure 5A–C depicts the histograms for the initial anisotropy factors $\mathbf{g_0}$ obtained from measurements on noncrystallized, semicrystallized, and crystallized samples, respectively. A Gaussian normal distribution was fitted to the displayed

data. For all crystallization regimes, the distributions appear to be centered around zero, but with different full width at half maximum (FWHM). We emphasize that the variation of the results presented in Figure 5 is much larger than the resolution of our SHG-CD setup, which is typically about ± 0.01.

Figure 5A indicates that the FWHM is the lowest, when the crystallization of the sample is suppressed. In the previous section, we hinted that structural effects are reflected in SHG-CD measurements of the anisotropy factor. The broadening in Figure 5B,C can be assigned to the transition from an amorphous solid to a polycrystalline film of optically active crystals. On the scale of the laser spot, this means that a measured anisotropy factor does not solely originate from the enantiomeric excess of the sample, but will also be affected by the excess of growing optically active domains that do not necessarily represent the enantiomeric distribution.

Practically, this means that desorbing extremely fresh samples within a few minutes after preparation is considered to be ideal for the reliable inference of the enantiomeric excess from the optical activity. Figure 6A–C shows how the induced anisotropy factor $\Delta\mathbf{g}$ in the desorbed laser spot behaves over the desorption time for the three different crystallization states of the initially racemic sample. The intensity of the desorption pulse was about 0.5 TW cm^{-2}. Our earlier study showed that the emergence of optical activity from the racemate is temporally confined to the first 10 min of desorption.[16] After that, the measured $\mathbf{g}$-value does not significantly change any more. This observation is reconfirmed by Figure 6B. For semicrystallized samples, the average achieved anisotropy factor amounts to $\Delta\mathbf{g} = 0.08 \pm 0.03$.

Figure 6C shows the evolution of $\Delta\mathbf{g}$ during laser desorption of crystallized samples. As discussed above, crystallized samples cannot be reliably probed via SHG-CD, because either sign of optical activity can arise during crystallization. The data suggest that crystallization obscures the inference of the anisotropy factor from time-dependent SHG-CD measurements, where initial structural fluctuations in the sample have been considered in the measurement of $\Delta\mathbf{g}$.
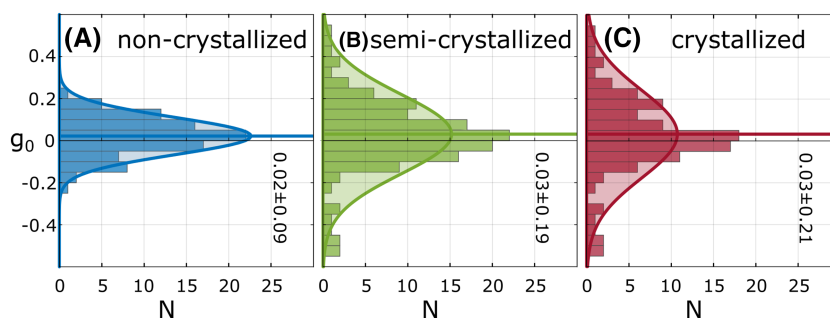
FIGURE 5 Influence of the crystallization on the reproducibility of the second harmonic generation circular dichroism (SHG-CD) measurement quantified by the initial anisotropy factor $\mathbf{g_0}$. (A) Noncrystallized samples, (B) semicrystallized samples, and (C) crystallized samples

non-crystallized

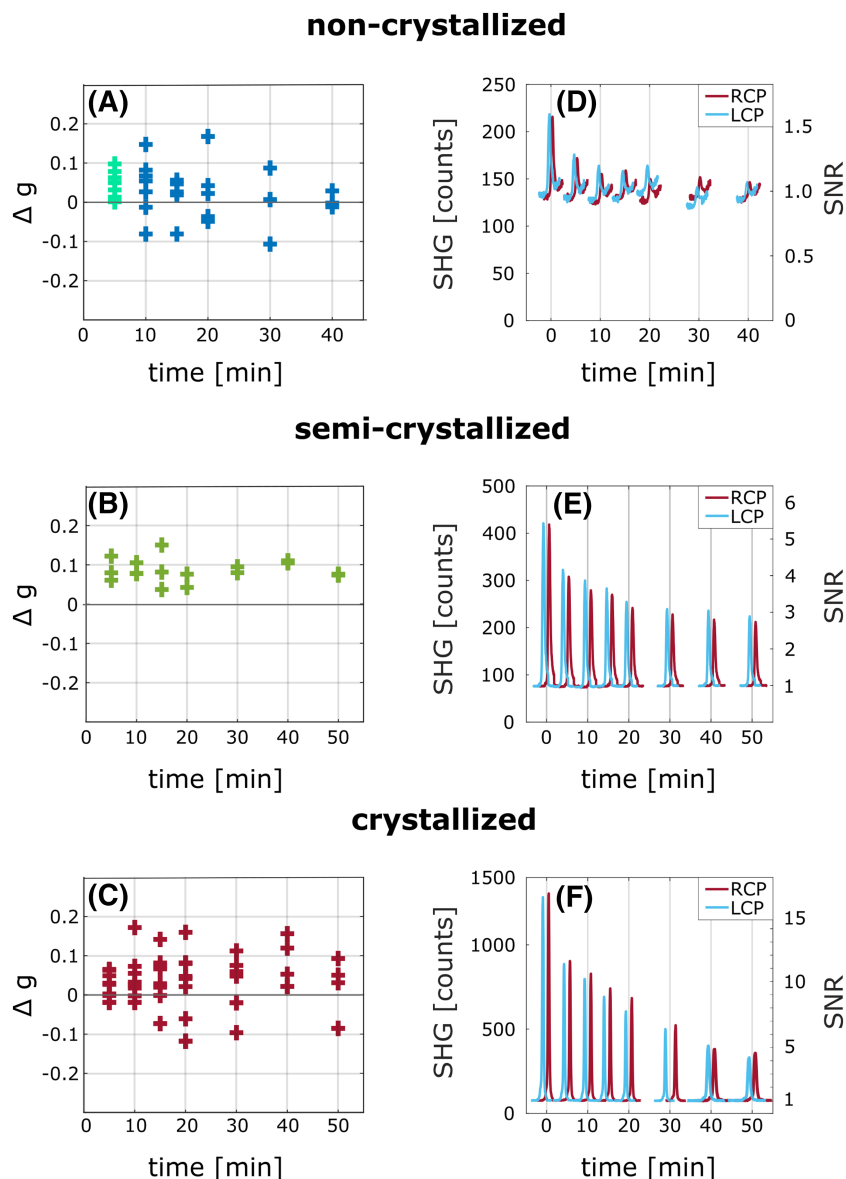

semi-crystallized

crystallized

FIGURE 6 First column: Influence of the crystallization state of the racemic sample on the change of the anisotropy factor Δg induced by laser desorption with circular polarized light at 650 nm. Second column: Typical second harmonic generation (SHG) spectra for right circular polarized (RCP) and left circular polarized (LCP) light, at 325-nm central wavelength and the signal to-noise-ratio (SNR). (A), (D) noncrystallized, (B), (E) semicrystallized, and (C), (F) crystallized

For illustrative purposes, typical RCP and LCP spectra for each time step are displayed in Figure 6D–F, from which Δg was determined by spectral integration over the SHG signal for each time step. We note that the typical spectral width of the SHG signal was $\Delta\lambda_{SHG} = 25$ nm (see Figure S1B). Here, $\Delta\lambda_{Fund}/\Delta\lambda_{SHG} \approx 3.1$, which is close to the expected value of $2\sqrt{2}$.[41] The decay of the SHG intensities over time is observed independent of the crystallization state of the sample. The decay indicates successful removal of material, as the SHG response of the sample is depending on its thickness.[16,31]

For further discussion, it must be noted that for semicrystallized (Figure 6E) and crystallized samples (Figure 6F), the SNR suffices to reliably determine the change in anisotropy factor over time Δg (t). Extrapolating the data from Figure 4B towards vanishing irradiation intensity, the nonlinear response from a completely

noncrystallized sample is expectedly low. This is why, for noncrystallized samples (Figure 6D), SNR approaches 1, especially after the sample has been desorbed for a while. That is also a reasonable explanation, why the measured induced anisotropy factor on noncrystallized samples (Figure 6A) amounts to $\Delta g = 0.02 \pm 0.07$. The large uncertainty indicates that due to low SNR, the resolution limit for the measurement of the enantiomeric excess is reached.

On a last note, we point out that, for the data points measured on noncrystallized samples at 5 min (cyan in Figure 6A), the SNR seems to be sufficient, to determine the values of Δg reliably. The measured anisotropy factor matches the sign of CD at the given wavelength.[16] For measurements with SNR < 1.3 however, the sensitivity of the measurements is not high enough to reliably measure the induced anisotropy factor.

3.4 | Influence of the laser intensity on the LD process

In this part, we present a quantitative investigation of the influence of the pulse intensity I_P on the induced anisotropy factor Δg, on the basis of the sample structure investigations and its influence on the nonlinear response and the optical activity generated in the sample. To this end, we systematically altered the intensity and c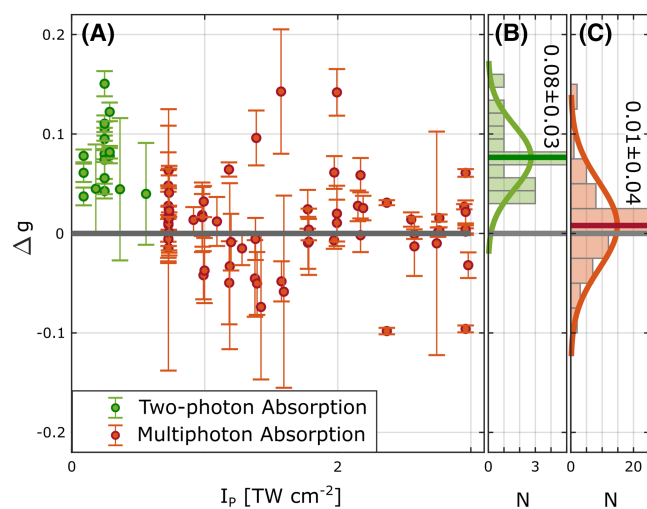alculated the values of Δg from the SHG intensities for different circular polarizations via Equation 1, after the sample has been irradiated with RCP light for at least 5 min.

Figure 7A depicts the induced anisotropy factor after the desorption, plotted over the pulse intensity of the incident light. The presented data were recorded from Δg measurements on semicrystallized samples, because reliable measurement of the induced anisotropy is limited to this regime. Upon an increase of I_P, two intensity regimes materialize. Below 0.7 TW cm^{-2}, the generated anisotropy factor is unidirectional and reproducible in accordance with our previous study.[16] Positive values for the anisotropy factor values emerge in the sample, as expected from irradiation with RCP light and resonant TPA. For completeness, we emphasize here again that this notion strongly indicates a quantum-mechanical contribution to the desorption process that has yet to be understood.

Interestingly, as I_P is further increased, a decline in the measured Δg values is recorded. Moreover, we denote a drastic increase of the data point scattering, even towards negative values of Δg. The threshold of the regime change appears to be at approximately $I_{th} \approx 0.7$ TW cm^{-2}, above which we observe single outliers with relatively high absolute values of Δg. Statistical analysis of all data points within both regimes reveals that in the low-intensity regime, the distribution curve averages at $\Delta g = 0.08 \pm 0.03$ (Figure 7B), whereas it amounts to $\Delta g = 0.01 \pm 0.04$ for $I_P > I_{th}$ (Figure 7C). The latter indicates a complete breakdown of the specific desorption for pulse intensities above I_{th}. As the peak intensity is the only control parameter of this measurement, this points towards the onset of multiphoton absorption of higher orders in the sample leading to

FIGURE 7 (A) Change in anisotropy factors Δg measured for different peak intensities of the desorption pulses. The colors represent desorption in the two-photon absorption regime (green) and the multiphoton absorption regime (red). (B) Histogram of the observed Δg for measurements in the green regime. (C) Histogram of the cumulative Δg for measurements in the red regime

FIGURE 8 Typical confocal microscopy images of the laser spots for two-photon absorption (A) and multiphoton absorption (B). (C) Profile through the data shown in (A). (D) Reflection light microscopy image of the laser spot shown in (A). (E) Reflection light microscopy image of the image of the spot in (B). The dark region in the middle of (E) indicates film degradation in the multiphoton absorption regime. The film degradation makes the height profiling with confocal microscopy unreliable
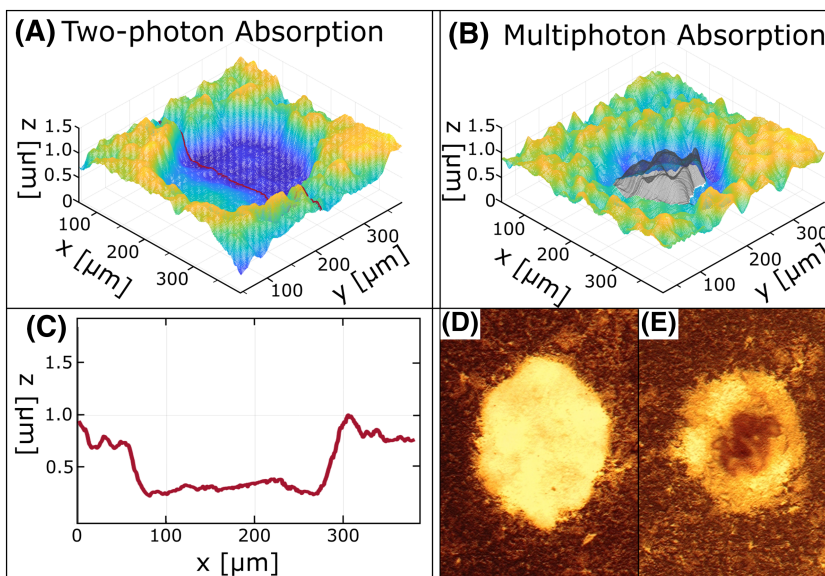
photo-degradation of the molecular structure. Given that the sample is transparent at the fundamental frequency, the lowest excitation mechanism is TPA. Thus, the existence of an upper limit for the intensity is an important hint. It indicates that the desorption's selectivity feature can break down for higher order absorption.

In order to gain a deeper understanding, we coupled the intensity-dependent measurements of the induced optical activity with confocal microscopy measurements of the desorption spots. Figure 8A,B depicts the typical retrieved confocal microscopy images of approximately 1-μm thin films, after they have been irradiated for more than 60 min. The respective reflection light microscopy images of the laser spots displayed in Figure 8A,B can be seen in Figure 8D,E, respectively.

The phenomenological model presented in our recent work allows both enantiomers to desorb from the surface at different rates and bulk molecules are only allowed to desorb after they have diffused to the surface.[16] The diffusion is enhanced by local heating from TPA in the bulk. According to the model, desorption takes place in a layer-by-layer manner. In the TPA regime, the confocal microscopy image (Figure 8A) and the height profile through the laser desorbed region (Figure 8C) show that the thin film has been partially depleted in the laser spot region, in agreement with this model. The second harmonic is generated from the remaining material in the laser spot which enables determination of $\Delta\mathbf{g}$ during the desorption.

The geometry of the desorption spot's crater further supports the claim that thermal desorption is mostly bypassed in the TPA-regime, as it is expected by irradiation with ultrashort laser pulses. The spot's appearance does not resemble the geometry of the Gaussian beam profile, as it is commonly seen for long-pulse ablation processes, which are dominated by thermal processes.[42] Instead, we observe a relatively flat crater with only a tiny crown at its edge area. In addition to the thermal desorption, which can never be bypassed, the model suggests that a quantum-mechanical channel in the sample is opened up. The reflection-light microscopy image in Figure 8D additionally supports this notion. Here, the laser spot appears to be sharp edged and highly transmissive, indicating the removal of material.

Because of the high amounts of energy deposited in the sample during multiphoton absorption, we observe a change in the laser spot geometry as the pulse intensity is further increased. Typically, the laser spots show similar geometry near the edge area, where the local energy input is much smaller than in the center. The crucial difference is that a defect region in the center of the laser spot emerges, subsequently referred to as "dark spot" (see Figure 8B,E). Guy et al. have observed that in the case of linear absorption with UV light, photo-degradation,

including fragmentation and combustion, arise at peak intensities as low as 0.8 TW cm^{-2}.[43] Especially in the center of the Gaussian beam profile, the local energy input per time is exceptionally high, thus making nonlinear effects of higher order especially dominant right in the center of the laser spot. Hence, the failure to generate significant $\Delta\mathbf{g}$ for large values of $\mathbf{I_P}$ might be caused by destruction of the molecules and loss of chiroptical character. A second effect mentioned in their work that also completely counteracts the generation of optical activity is photo-switching of the enantiomers as they undergo a dihedral angle rotation, that is, photo-racemization. The given threshold is obviously greatly exceeded by the fundamental pulse intensities $\mathbf{I_P}$ used to irradiate the sample. We emphasize though that the linear absorption coefficient almost vanishes at the chosen wavelength. Also, the TPA cross section in the BINOL film is orders of magnitudes lower than the linear UV cross section.[44] Therefore, the photo-degradation and photo-racemization threshold is considerably higher than for linear UV absorption.[45]

The dark spot is a highly absorptive region, and its presence completely changes the local absorption properties of the film. The light–matter interaction in this case is largely dominated by linear absorption in the visible range, which means that vast amounts of thermal energy are being deposited in the film. Supposedly, when the dark spot is present in the film, thermal desorption in this regime cannot reliably be bypassed anymore and dominates the desorption dynamics as a whole. Thermal desorption is enantiomerically unspecific as it lacks the additional degree of freedom otherwise given by the handedness of the light. This adequately explains the scattering of $\Delta\mathbf{g}$ around zero in Figure 7A, when $\mathbf{I_{th}}$ is exceeded. The selective removal of material in this case can be considered as a purely statistical process, spontaneously generating large values for the anisotropy factor in the sample, but averaging approximately zero.

Looking back at Figure 7A, we can note an increased statistical uncertainty of the data points in the multiphoton absorption regime, which until now has not been pointed out yet. Single data points have been recorded by averaging >10 alternatingly measured SHG spectra for each polarization to retrieve $\mathbf{I^{LCP}}$ and $\mathbf{I^{RCP}}$. A possible explanation for the increased uncertainty could be that the size of the dark spot evolved over time. This particularly affects the effective area in which the second harmonic can be generated. When the morphology of the dark spot changes uncontrollably during the measurement, the sensitivity of the measurement becomes unpredictable. The average resolution of the $\Delta\mathbf{g}$ measurement increases upon the exceedance of $\mathbf{I_{th}}$ from ±0.01 to ±0.03.

4 | CONCLUSION AND OUTLOOK

This contribution highlights recent developments in the understanding of laser desorption of chiral molecules with CPL. First, we performed surface roughness measurements of racemic BINOL samples in order to define the crystallization state of the sample and coupled those measurements to reflection microscopy and SEM. On the basis of this classification, we conducted structural analysis of racemic and enantiopure BINOL films via polarization resolved microscopy, allowing us to display optically active domains in the sample. By systematic suppression of the sample's crystallization, an increased reproducibility was achieved. With regard to up-scaling of the process, a narrower distribution of g_0 greatly increases reproducibility. We specifically note the drawbacks of full crystallization regarding the quality and reliability of inducing optical activity in racemic samples. One key observation here is that the macroscopic optical activity does not reflect the enantiomeric distribution in the sample when the sample is crystallized.

On the other hand, full suppression of crystallization counteracts the sensitivity of the Δg measurement. We find that the SHG intensity is greatly decreased for non-crystallized samples, even going so far that the SNR becomes insufficient for reliable retrieval of the anisotropy factors. This issue may be resolved by employing photo-detector devices with higher sensitivities that are capable of measuring single SHG photons. All together, we can confidently state that for the induction of optical activity and moreover the selective separation of enantiomers in the film, asymmetric laser desorption must be performed on freshly prepared thin films, before the onset of crystallization. In this work, we weighed the limited resolution of the measurement up by measuring on semicrystallized films.

Moreover, pulse intensity-dependent measurements on generation of anisotropy factor revealed a threshold value for the onset of multiphoton absorption. Below $I_{th} \approx 0.7$ TW cm^{-2}, we observe a reliable induction of optical activity in the racemic sample via resonant TPA of CPL. This notion unambiguously reconfirms our results presented in our earlier report.[16] Above the threshold, a near-zero average value for the induced anisotropy factor was measured. The possible reasons for this are manifold, yet a comprehensive study of the confocal microscopy images of laser spots in both regimes showed the generation of dark spots, arising only when the multiphoton threshold is exceeded. These defects not only impair the measurement of the anisotropy factor but also alter the microscopic mechanisms of desorption.

Our investigations indicate that although crystallization of the film does affect the reliability of the observed anisotropy factor generated by asymmetric laser desorption, it cannot explain the clear correlation of the sign of the observed anisotropy factor with the handedness of the laser pulse used for desorption. This conclusion points further in the direction of enantiomeric excess in the remaining film to be responsible for the observed optical activity, although it does not provide hard evidence. The possibility of generating enantiomeric excess in a racemic film by means of light provides us with a flexible and contamination-free method for enantiomeric enrichment of racemic films. Implementing such a method in a cyclic approach of film-deposition and asymmetric desorption might even allow for an enantio-purification approach, highly demanded in the pharmaceutical industry.

DATA AVAILABILITY STATEMENT
The data that support the findings of this study are available from the corresponding author upon reasonable request.

ORCID
Aras Kartouzian https://orcid.org/0000-0002-2193-2902

REFERENCES

1. Bailey J, Chrysostomou A, Hough J, et al. Circular polarization in star-formation regions: implications for biomolecular homochirality. *Science*. 1998;281(5377):672-674.
2. Blackmond DG. The origin of biological homochirality. *Cold Spring Harb Perspect Biol*. 2010;2(5):a002147-1-a002147-17.
3. Fujii N, Saito T. Homochirality and life. *The Chemical Record*. 2004;4(5):267-278.
4. Mason S. Biomolecular homochirality. *Chem Soc Rev*. 1988;17: 347-359.
5. Chen X, Huang Z, Chen S-Y, Li K, Yu X-Q, Pu L. Enantioselective gel collapsing: a new means of visual chiral sensing. *J am Chem Soc*. 2010;132(21):7297-7299.
6. Frishman E, Shapiro M, Gerbasi D, Brumer P. Enantiomeric purification of nonpolarized racemic mixtures using coherent light. *J Chem Phys*. 2003;119(14):7237-7246.
7. Kartouzian A. Spectroscopy for model heterogeneous asymmetric catalysis. *Chirality*. 2019;31(9):641-657.
8. Mikami K, Matsukawa S. Asymmetric synthesis by enantiomer-selective activation of racemic catalysts. *Nature*. 1997;385(6617):613-615.

9. Noyori R. Asymmetric catalysis: science and opportunities (Nobel lecture). *Angew Chem Int Ed*. 2002;41(12):2008-2022.

10. Medina E, González-Arraga LA, Finkelstein-Shapiro D, Berche B, Mujica V. Continuum model for chiral induced spin selectivity in helical molecules. *J Chem Phys*. 2015;142(19):194308-1-194308-6.

11. Naaman R, Waldeck DH. Chiral-induced spin selectivity effect. *The Journal of Physical Chemistry Letters*. 2012;3(16):2178-2187.

12. Qi D, Kenaan A, Cui D, Song J. Novel insights into the selection to electron's spin of chiral structure. *Nano Energy*. 2018;52:142-152.

13. Quack M, Stohner J. Parity violation in chiral molecules. *CHIMIA Int J Chem*. 2005;59(7–8):530-538.

14. Quack M, Stohner J, Willeke M. High-resolution spectroscopic studies and theory of parity violation in chiral molecules. *Annu Rev Phys Chem*. 2008;59:741-769.

15. von Weber A, Hooper DC, Jakob M, Valev VK, Kartouzian A, Circular Dichroism HU. Isotropy–polarity reversal of ellipticity in molecular films of 1, 1′-bi-2-Naphtol. *ChemPhysChem*. 2019;20(1):62-69.

16. Mortaheb F, Oberhofer K, Riemensberger J, et al. Enantiospecific desorption triggered by circularly polarized light. *Angew Chem Int Ed*. 2019;58(44):15685-15689.

17. Kauranen M, Verbiest T, Van Elshocht S, Persoons A. Chirality in surface nonlinear optics. *Opt Mater*. 1998;9(1–4):286-294.

18. Kauranen MM, Verbiest T, Persoons A, et al. Chiral effects in the second-order optical nonlinearity of a poly (isocyanide) monolayer. *Adv Mater*. 1995;7(7):641-644.

19. Petralli-Mallow T, Wong T, Byers J, Yee H, Hicks J. Circular dichroism spectroscopy at interfaces: a surface second harmonic generation study. *J Phys Chem*. 1993;97(7):1383-1388.

20. Verbiest T, Kauranen M, Persoons A, Ikonen M, Kurkela J, Lemmetyinen H. Nonlinear optical activity and biomolecular chirality. *J am Chem Soc*. 1994;116(20):9203-9205.

21. Aakeröy CB, Beatty AM. Crystal engineering of hydrogen-bonded assemblies—a progress report. *Australian Journal of Chemistry*. 2001;54(7):409-421.

22. Desiraju GR. The C—H⋯ O hydrogen bond: structural implications and supramolecular design. *Acc Chem Res*. 1996;29(9):441-449.

23. Mori K, Masuda Y, Kashino S. (+)-(R)-and racemic forms of 2, 2′-dihydroxy-1, 1′-binaphthyl. *Acta Crystallographica Section C: Crystal Structure Communications*. 1993;49(6):1224-1227.

24. Kuroda R, Mason SF. The crystal and molecular structure of R-(−)-1, 1′-binaphthyl: the conformational isomerism and a comparison of the chiral with the racemic packing mode. *Journal of the Chemical Society, Perkin Transactions*. 1981;2(1):167-170.

25. Maria TM, Marins FA, Costa JBS, et al. Solid state investigation of BINOL and BINOL derivatives: a contribution to enantioselective symmetry breaking by crystallization. *Thermochimica Acta*. 2017;648:32-43.

26. Sahnoun R, Koseki S, Fujimura Y. Theoretical investigation of 1, 1′-bi-2-naphthol isomerization. *J Mol Struct*. 2005;735:315-324.

27. Lee T, Peng JF. Photoluminescence and crystal structures of chiro-optical 1, 1′-bi-2-naphthol crystals and their inclusion compounds with dimethyl sulfoxide. *Cryst Growth des*. 2010;10(8):3547-3554.

28. Heffner G, Dahman S, Pearson D, Gettinger C. The effect of molecular weight and crystallinity on the conductivity of a conducting polymer. *Polymer*. 1993;34(15):3155-3159.

29. Sullivan EM, Oh YJ, Gerhardt RA, Wang B, Kalaitzidou K. Understanding the effect of polymer crystallinity on the electrical conductivity of exfoliated graphite nanoplatelet/polylactic acid composite films. *Journal of Polymer Research*. 2014;21(10):563-1-563-9.

30. An G, Yan P, Sun J, Li Y, Yao X, Li G. The racemate-to-homochiral approach to crystal engineering via chiral symmetry breaking. *CrstEngComm*. 2015;17(24):4421-4433.

31. Heister P, Lünskens T, Thämer M, et al. Orientational changes of supported chiral 2, 2′-dihydroxy-1, 1′ binaphthyl molecules. *Phys Chem Chem Phys*. 2014;16(16):7299-7306.

32. von Weber A, Jakob M, Kratzer E, Kartouzian A, Heiz U. In situ second-harmonic generation circular dichroism with submonolayer sensitivity. *ChemPhysChem*. 2019;20(1):134-141.

33. Dutta S, Gellman AJ. Enantiomer surface chemistry: conglomerate versus racemate formation on surfaces. *Chem Soc Rev*. 2017;46(24):7787-7839.

34. Kissick DJ, Wanapun D, Simpson GJ. Second-order nonlinear optical imaging of chiral crystals. *Annu Rev Anal Chem*. 2011;4:419-437.

35. LeCaptain DJ, Berglund KA. The applicability of second harmonic generation for in situ measurement of induction time of selected crystallization systems. *J Cryst Growth*. 1999;203(4):564-569.

36. Wanapun D, Kestur US, Kissick DJ, Simpson GJ, Taylor LS. Selective detection and quantitation of organic molecule crystallization by second harmonic generation microscopy. *Anal Chem*. 2010;82(13):5425-5432.

37. Franken EP, Hill AE, Peters C, Weinreich G. Generation of optical harmonics. *Phys Rev Lett*. 1961;7(4):118-119.

38. Byers J, Yee H, Hicks J. A second harmonic generation analog of optical rotatory dispersion for the study of chiral monolayers. *J Chem Phys*. 1994;101(7):6233-6241.

39. Byers J, Yee H, Petralli-Mallow T, Hicks J. Second-harmonic generation circular-dichroism spectroscopy from chiral monolayers. *Physical Review B*. 1994;49(20):14643-14647.

40. Ozcelik A, Pereira-Cameselle R, Von Weber A, et al. Device-compatible chiroptical surfaces through self-assembly of enantiopure allenes. *Langmuir*. 2018;34(15):4548-4553.

41. Ehmke T, Knebl A, Reiss S, et al. Spectral behavior of second harmonic signals from organic and non-organic materials in multiphoton microscopy. *AIP Advances*. 2015;5(8):084903-1-084903-6.

42. Semerok A, Salle B, Wagner J-F, Petite G. Femtosecond, picosecond, and nanosecond laser microablation: laser plasma and crater investigation. *Laser and Particle Beams*. 2002;20(1):67-72.

43. Guy S, Bensalah-Ledoux A, Lambert A, Guillin Y, Guy L, Mulatier J. Chiral organic thin films: how far pulsed laser deposition can conserve chirality. *Thin Solid Films*. 2012;520(20):6440-6445.

44. Vesga Y, Hernandez FE. Study of the effect of the pulse width of the excitation source on the two-photon absorption and two-photon circular dichroism spectra of biaryl derivatives. *Chem a Eur J*. 2016;120(34):6774-6779.

45. Taupier G, Boeglin A, Crégut O, et al. Beating photo-degradation in sum-frequency imaging of chiral organic media. *Opt Mater.* 2015;45:22-27.

SUPPORTING INFORMATION

Additional supporting information may be found online in the Supporting Information section at the end of this article.